Electronic Supplementary Material (ESI) for Physical Chemistry Chemical Physics.

Induction-heated ball-milling: a promising asset for mechanochemical reactions

Gautier Félix,[1,*] Nicolas Fabrègue,[1] César Leroy,[1] Thomas-Xavier Métro,[1]

Chia-Hsin Chen,[1,2] Danielle Laurencin[1,*]

1. ICGM, CNRS, Université de Montpellier, ENSCM, Montpellier, France
2. Current affiliation: Johnson Matthey Technology Centre, Blount's Court, Sonning Common, Reading, RG4 9NH, United Kingdom

Supporting information

Table of contents

I- Mechanochemistry equipment and induction heating set-up 2
a/ Milling equipment 2
b/ Induction heating set-up 3
c/ Thermal analysis 3
d/ Reproducibility tests and influence of vertical movements 4
e/ Experiments involving commercial ss@PTFE beads 5

II- Numerical simulations 6
a/ Computational details 6
b/ Complementary simulations 7
c/ Joule effect & hysteresis loss power heating 9
Eddy current & Joule effect (P_{ind} / I^2 dependency) 9
Hysteresis Power-Loss Heating (P_{hyst} / I^2 dependency) 12

III- Reactions performed using i-BM 14
a/ Reagents 14
b/ Milling and ^{17}O-enrichment of silica 14
c/ Hydrolysis of activated fatty acids 16
d/ Formation of "snowballs": synthesis of the leucine methyl ester-urea cocrystal 22

IV- More complete literature survey on combined heating & milling studies 23

I- Mechanochemistry equipment and induction heating set-up

a/ Milling equipment

The majority of the mechanochemical syntheses were performed with a Fritsch Pulverisette-23 (P23) vertical mixer mill, using 10 mL inner-volume jars made of Perspex (PMMA polymer) or stainless-steel (noted ss), with 10 mm diameter ss beads in most cases. Core shell ss@PTFE beads (10 mm diameter) were also used in some tests. Induction heating ball-milling experiments (i-BM) were performed with this milling equipment, as shown in Figure S1.

Complementary reactions were also performed using an MM400 Retsch mixer mill (for the activation of fatty acids), as further detailed in section III-c of this document.

In this work, the terms ball/bead, and reactor/jar are used with no specific distinction.

a/ Top view

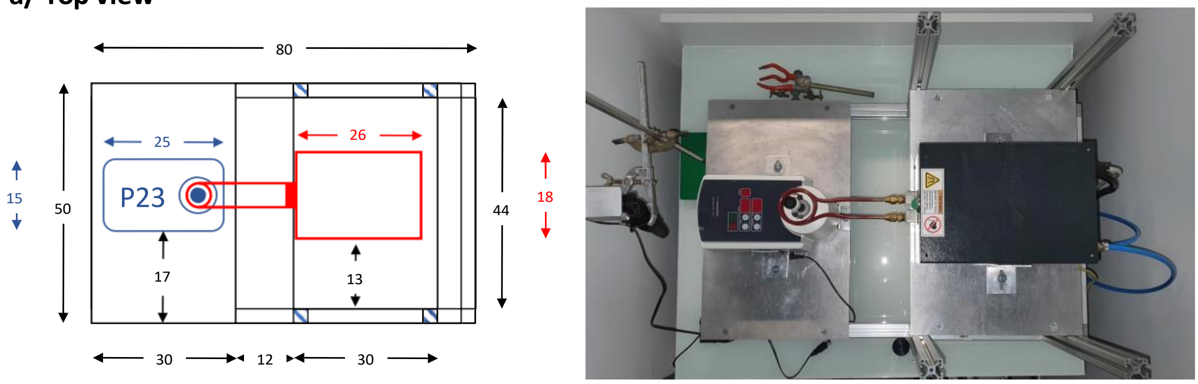

b/ Side view

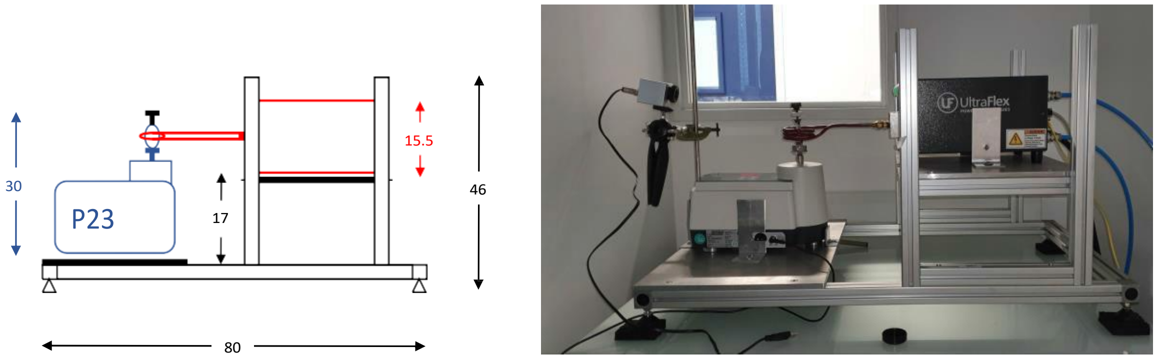

Figure S1. Photos and technical drawing of the set-up used for the i-BM experiments. The dimensions reported on the left are in cm.

b/ Induction heating set-up

The induction heating was carried out using the UPT-n2 Nano Lite System for Nanoparticle Research from the UltraFlex company.[1] This device is composed of a power supplier (generator connected to an amplifier and a capacitor/coil couple) and a water-cooling system. The current which propagates inside the coil can be adjusted from 0 to 320 A. The coil is composed of 3 rings with an internal diameter of 55 mm. The maximum calculated field at the coil centre is ≈20 mT (milliTesla). The working frequency used is the resonance frequency of the capacitor/coil couple. For this study we used a 1.0 µF capacitor, which leads to a resonance frequency of 161 kHz.

Jar / bead component	**Targeted Temperature**	**t_0**	**Current between t_0 and t_1**	**t_1**	**Current between t_1 and t_2**	**t_2**	**Current between t_2 and t_3**	**t_3**
{PMMA jar / ss bead}	T1 = 40 °C	0 s	50.0 A	22 s	11.0 A	120 s	x	x
	T2 = 60 °C	0 s	50.0 A	48 s	15.5 A	120 s	x	x
	T3 = 80 °C	0 s	50.0 A	70 s	21.0 A	120 s	x	x
{ss jar / ss bead}	T1 = 40 °C	0 s	50.0 A	15 s	9.0 A	120 s	x	x
	T2 = 60 °C	0 s	50.0 A	29 s	14.0 A	59 s	11.0 A	120 s
	T3 = 80 °C	0 s	50.0 A	47 s	17.5 A	60 s	12.5 A	120 s

Table S1. Experimental heating conditions used for both configurations {PMMA jar / ss bead} and {ss jar / ss bead}, at different moments of the heating process (noted t_0, t_1, t_2 and t_3). These parameters were also used in the simulations.

c/ Thermal analysis

An OPTRIS PI450i thermal imaging camera was used to carry out the temperature measurements. The optical resolution of the camera is 382 x 288 pixels. Three different temperatures were recorded every two seconds during the milling, corresponding to the top, centre and bottom of the jar at each time-point. The temperature accuracy measured using this system is estimated to ± 2°C. It is worth noting that due to the reflectivity of stainless steel in the IR domain, the thermal imaging temperature measurements on ss balls or beads were performed by positioning a sticker at the surface of the object, as shown in the zoom in Figure S2. Numerical simulations were carried out (see Figure S6 in section II of this document), showing that the temperature at the surface of the sticker is essentially the same (meaning that the presence of this sticker does not bias the conclusions drawn here). Moreover, a comparison of temperatures measured using this thermal imaging camera and a standard thermocouple is shown in Figure S2: a difference of less than 0.3 °C was found between the two.

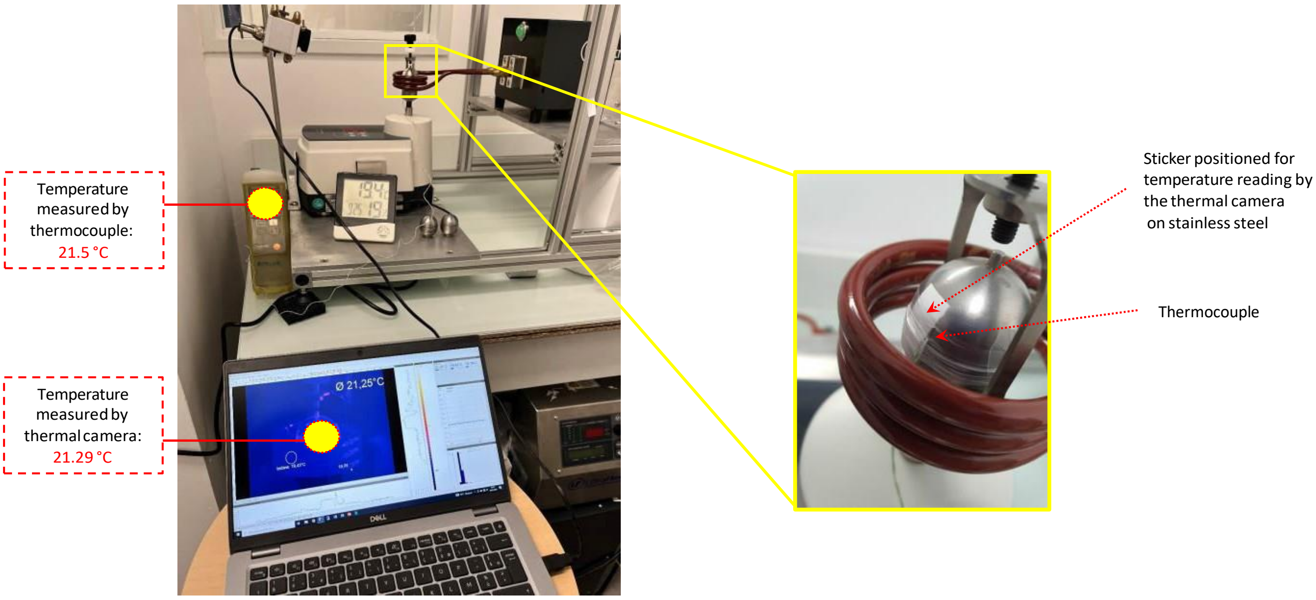

Figure S2. Comparison of temperature readings at the surface of a stainless steel reactor, when using the thermal imaging camera (pointing to the sticker), or a standard thermocouple (in direct contact with the ss jar).

d/ Influence of vertical movements on the ss jar's temperature

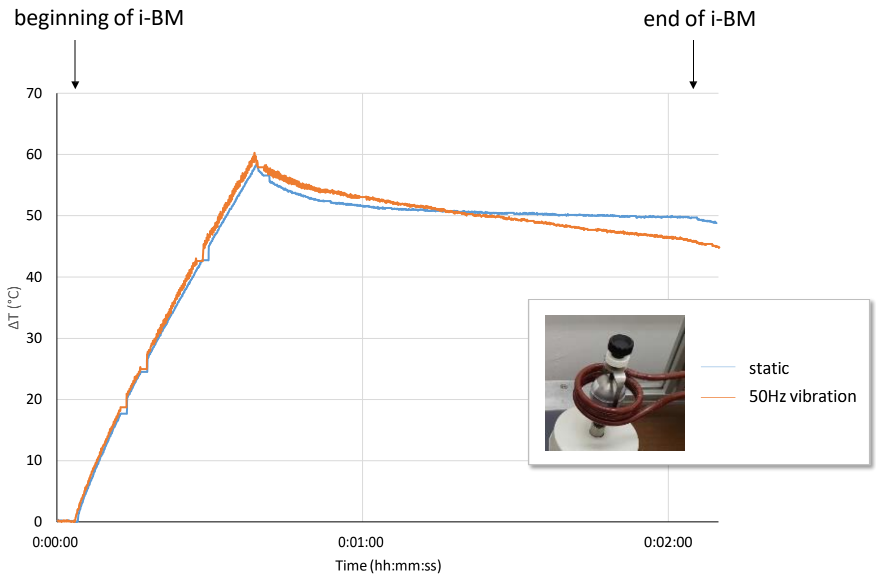

Figure S3. Influence of the vertical movement of the jar on the temperature reached during i-BM. Experiments were performed on an empty ss jar, over 2 minutes, using the exact same heating program. The difference in temperature ΔT achieved without vibrations (blue) and while vibrating vertically at 50Hz (orange) was found to be less than 5 °C. Such difference could potentially be corrected by adjusting the heating program (not tested at this stage).

e/ Reproducibility of the measurements

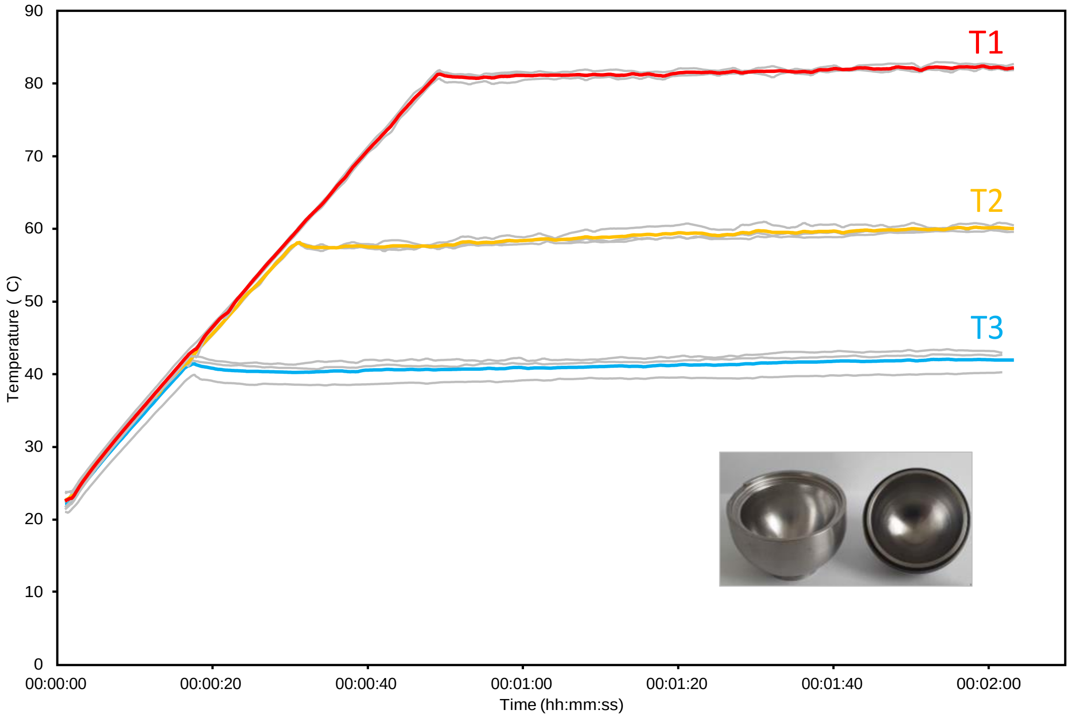

Figure S4. Reproducibility tests for 3 targeted heating temperatures (noted T1, T2, and T3), in the case of the ss jar heating by i-BM. For each temperature, experiments were performed 3 times (grey curves). The averaged results are then shown in red, yellow and blue.

f/ Experiments on commercial ss@PTFE beads

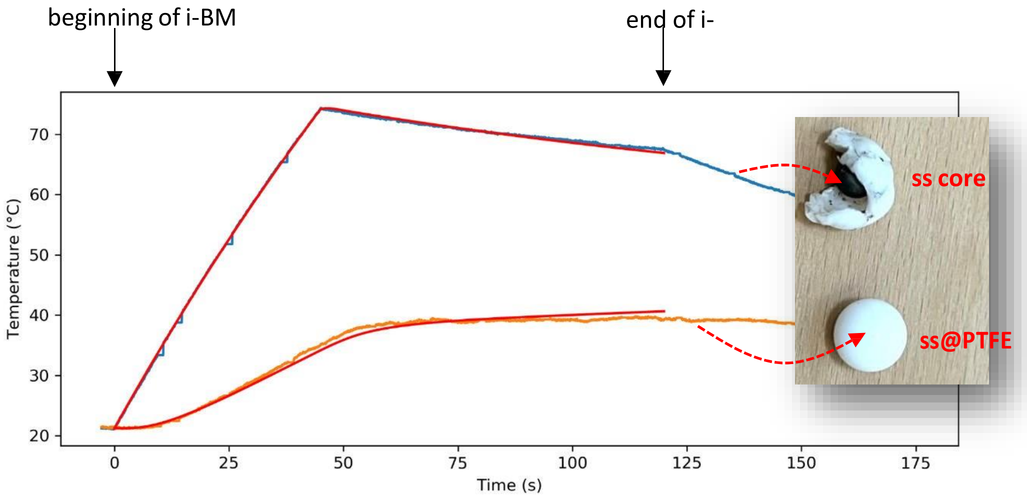

Figure S5. i-BM heating of a commercial core-shell ss@PTFE bead, placed on a PTFE-mat in the centre of the induction-coil (orange curve), in comparison to the heating of the ss core only (blue curve). Both systems were subject to the same induction-heating program, during 2 minutes. Under these conditions, a temperature ~40°C could already be achieved for the ss@PTFE bead. It should be noted that the temperature reached by the ss core suggests that its exact ss composition is different compared to the one of the other ss beads studied here (Figures 2 and 3). Red curves represent simulations in the same conditions compared to the experience (ss core only and ss@PTFE). The simulation process is described in the numerical simulations section of the supporting information.

II- Numerical simulations

a/ Computational details

Magnetic and magnetothermal simulations on {coils / jar / bead} system were performed using the COMSOL software. The Maxwell equations were solved to determine spatially the amplitude of the alternating magnetic field. The value of the magnetic field was used to calculate the heat power produced by hysteresis loss power and Joule effects. The heat power was injected in the heat equation, which was solved simultaneously with the simplified Navier–Stokes equation, to take into account the heat propagation and the convection term present for the air (as illustrated in Figure S7). In all cases, a 2D model with rotational symmetry was used in simulations, with dimensions for the bead, jar and coil similar to those used in experiments. The model consisted of a coil which is crossed by an electrical current, a jar which can be in PMMA, stainless-steel (ss), tungsten carbide or copper, and a fixed stainless-steel bead inside the jar.

To fit the experimental results (*i.e.* the heating curves shown in Figures 2 and 3 of the main text) a homemade python script was written. It used the mph library and the "curve_fit" function from the scipy.optimize library (least square fitting method). The current value and frequency were kept equal to those used experimentally, and the parameters which were optimized during the fit were the stainless-steel electrical conductivity, its heat capacity and its thermal conductivity.

The optimized parameters obtained for stainless-steel in different simulations are displayed in Table S2.

Jar / bead component	**Material**	**Electrical conductivity ($S.m^{-1}$)**	**Heat capacity ($J.kg^{-1}.K^{-1}$)**	**Thermal conductivity ($W.m^{-1}.K^{-1}$)**	**Figures**
{PMMA jar / ss bead}	PMMA*	0	1500.0	0.2	2b, 3a, 3b and 3f
	ss	$6.61 \cdot 10^6$	579.1	346.3	
{ss jar / ss bead}	ss	$7.72 \cdot 10^6$	805.9	17.6	2a, 3c, 3d, 3e and 3f
{Cu jar / ss bead}	Cu*	$60.0 \cdot 10^6$	385.0	400.0	3e
	ss	$6.61 \cdot 10^6$	579.1	346.3	
{WC jar / ss bead}	WC*	$18.2 \cdot 10^6$	203.2	110.0	3e
	ss	$6.61 \cdot 10^6$	579.1	346.3	
PTFE shell	PTFE	0	1642	0.38	S5

Table S2. Relevant parameters used in numerical simulations of Figures 2 and 3 (main text) and Figure S5 (ESI). Parameters of materials with * were not optimized during the fitting (they were taken from other databases, including from the COMSOL software).

b/ Complementary simulations

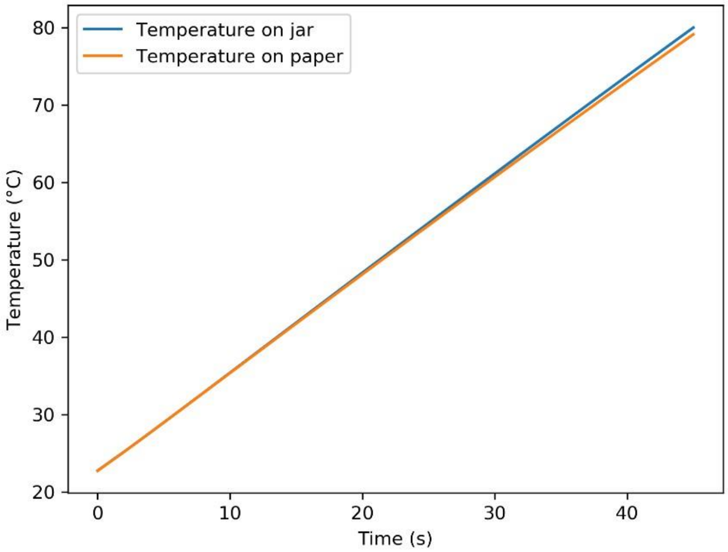

Figure S6. Simulations comparing the temperatures of the jar and of a piece of paper stuck on the jar's surface (as shown in Figure S2), in the case of the {ss jar / ss bead} system. The same simulation parameters as in Figure 2 (main text) were used here.

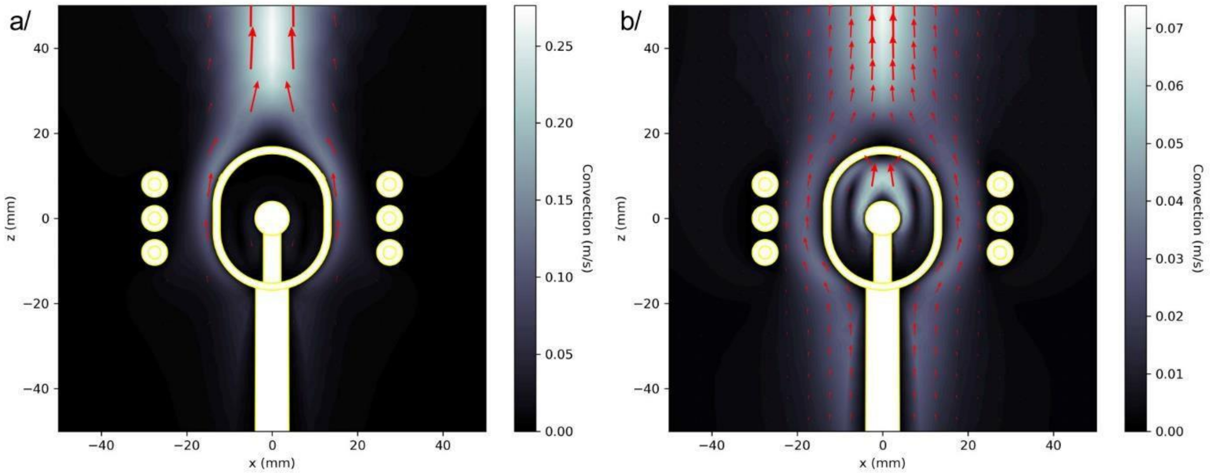

Figure S7. Air convection flow determined by the simulations, when the temperature reaches 80°C in the case of the {ss jar / ss bead} (a) and {PMMA jar / ss bead} (b) systems. In both cases, no vertical movement of the jar is considered in these simulations.

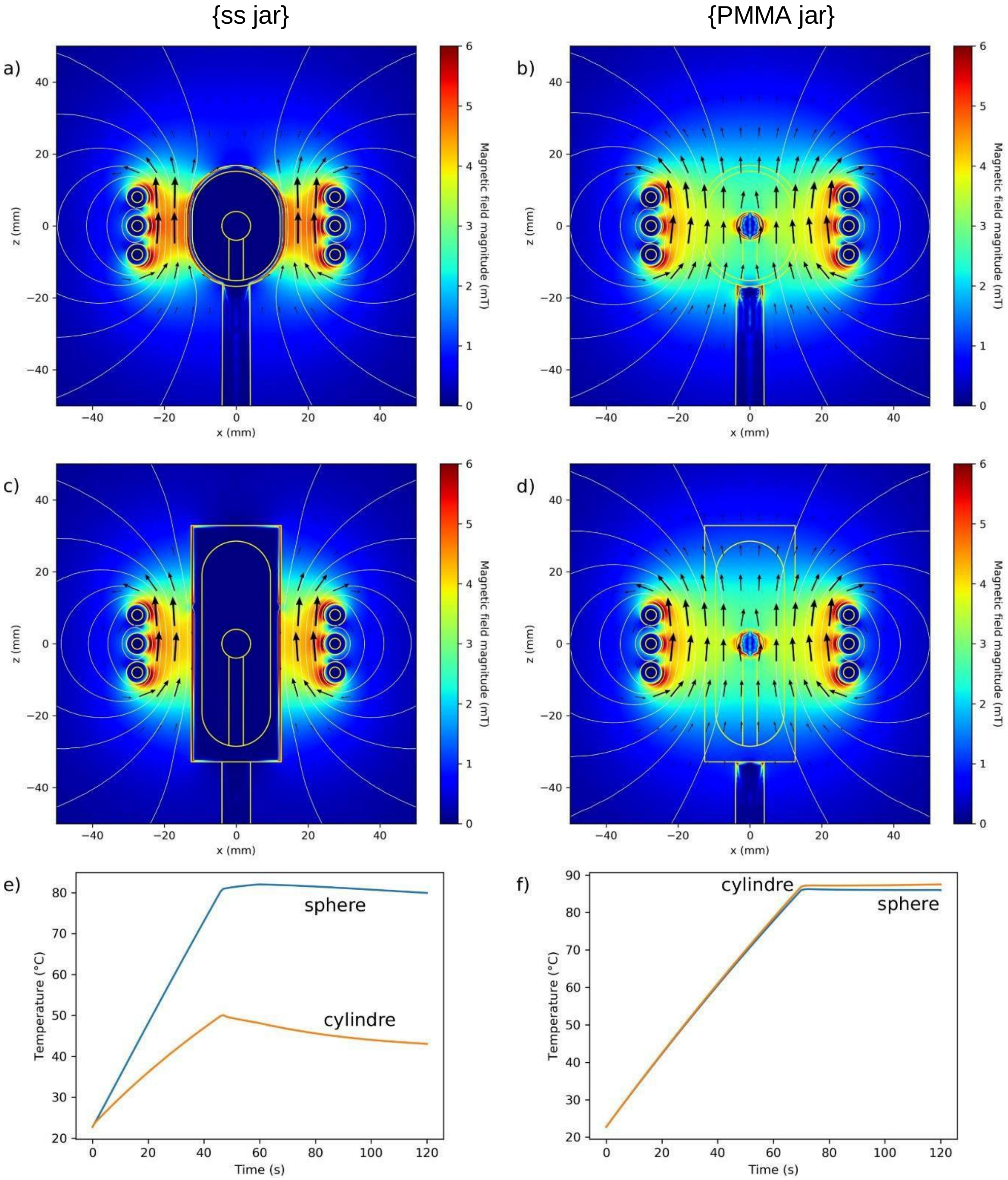

Figure S8. *Left:* Simulations showing the magnetic field lines ((a) and (c)), and the jar temperature (e) reached under similar i-BM heating conditions, when using ss jars of different geometry (spherical (a) vs cylindrical (c)). As expected for a material like ss, the jar, independently from its shape, screens the magnetic field. *Right:* Simulations showing the magnetic field lines and ss bead temperature (f) reached under similar i-BM heating conditions, when using PMMA jars of different geometry (spherical (b) vs cylindrical (d)). As expected for a material like PMMA (which does not screen the magnetic field), when placing the bead at the centre of the induction coil, no significant difference is noticeable when switching from one material to the other.

c/ Joule effect & hysteresis loss power heating

In Figure 3f of the article, the evolution of the heating rate ($\frac{\partial T}{\partial t}$) depends on I^2, with I the current propagating inside the coil. In adiabatic conditions, and with the approximation that all the medium has the same temperature, we can write:

$$\rho c_V \frac{\partial T}{\partial t} = P_{ind} + P_{hyst}$$

with P_{ind} the power produced by the Joule effect, P_{hyst} the power produced by the hysteresis loss power, ρ the medium mass density, and c_V the medium heat capacity.

The solution of this equation is:

$$T(t) = T_0 + \frac{P_{ind} + P_{hyst}}{\rho c_V} t$$

with T_0 the initial temperature.

From these late equations we can conclude that the P_{ind} and P_{hyst} should have a I^2 dependency. This relationship is derived below.

Eddy current & Joule effect (*P_{ind}* / I^2 dependency):

The electrical field produced by induction is written as follows:

$$\vec{E}_{ind} = -\frac{\partial A}{\partial t} + v \wedge \vec{B}$$

with A the magnetic vector potential, v the velocity of the conductor and $\vec{B}$ the magnetic field.

In our case we have $v = 0$. Which means:

$$\vec{E}_{ind} = -\frac{\partial A}{\partial t}$$

The magnetic vector potential depends on the coils current:

$$A(r,t) = \frac{\mu_0}{4\pi} \iiint_V \frac{J(\vec{r'}, t')}{|r - \vec{r'}|} \, \mathrm{d}^3\vec{r'}$$

with t' the retarded time:

$$t' = t - \frac{|r - \vec{r'}|}{c}$$

with c the light velocity.

In our configuration the current can be approximated as:

$$J(t) = J_0 \cdot \cos(\omega t) \cdot \vec{e_\theta}$$

Then:

$$J(t') = J_0 \cdot \cos\left(\omega t - \omega \frac{|r - \vec{r'}|}{c}\right) \cdot \vec{e_\theta}$$

$$J(t') = J_0 \cdot \left(\cos(\omega t)\cos\left(\omega \frac{|r - \vec{r'}|}{c}\right) + \sin(\omega t)\sin\left(\omega \frac{|r - \vec{r'}|}{c}\right)\right) \cdot \vec{e_\theta}$$

Then the magnetic vector potential becomes:

$$A(r,t) = J_0 \cdot \vec{e_\theta} \cdot \frac{\mu_0}{4\pi} \left(\cos(\omega t) \iiint_V \frac{\cos\left(\omega \frac{|r - \vec{r'}|}{c}\right)}{|r - \vec{r'}|} \, \mathrm{d}^3\vec{r'} + \sin(\omega t) \iiint_V \frac{\sin\left(\omega \frac{|r - \vec{r'}|}{c}\right)}{|r - \vec{r'}|} \, \mathrm{d}^3\vec{r'} \right)$$

If we define two time constants $c_r(r)$ and $c_i(r)$ as:

$$c_r(r) = \iiint \frac{\cos\left(\omega \frac{|r - \vec{r'}|}{c}\right)}{|r - \vec{r'}|} \, \mathrm{d}^3\vec{r'}, \quad c_i(r) = \iiint \frac{\sin\left(\omega \frac{|r - \vec{r'}|}{c}\right)}{|r - \vec{r'}|} \, \mathrm{d}^3\vec{r'}$$

$$V \qquad |r - \vec{r}'| \qquad\qquad V \qquad |r - \vec{r}'|$$

Then the magnetic vector potential becomes:

$$A(r,t) = J_0 \cdot \frac{\mu_0}{4\pi}\left(c_r(r)\cdot\cos(\omega t) + c_i(r)\cdot\sin(\omega t)\right)\cdot\vec{e}_\theta$$

The electrical field produced by induction in the conductor is:

$$\vec{E}_{ind} = -\frac{\partial}{\partial t}\left(J_0\cdot\frac{\mu_0}{4\pi}\left(c_r(r)\cdot\cos(\omega t) + c_i(r)\cdot\sin(\omega t)\right)\right)\cdot\vec{e}_\theta$$

$$\vec{E}_{ind} = -J_0\cdot\frac{\mu_0}{4\pi}\omega\left(c_i(r)\cdot\cos(\omega t) - c_r(r)\cdot\sin(\omega t)\right)\cdot\vec{e}_\theta$$

Using the Ohm law, the electrical field produced by induction can be written using the volumic current J_{ind} and the volumic resistivity ρ:

$$\vec{E}_{ind} = \rho J_{ind}$$

We can conclude that J_{ind} is directly proportional to the amplitude of the current propagating in the coils (J_0).

The local heat power produced by Joule effect due to inducted volumic currents is:

$$p_{ind} = \frac{1}{T}\int_0^T J_{ind}\cdot\vec{E}_{ind}\,\mathrm{d}t$$

$$p_{ind} = \frac{\rho}{T}\int_0^T J_{ind}^2\,\mathrm{d}t$$

As $J_{ind} \propto J_0$, then we can conclude:

$$p_{ind} \propto J_0^2$$

and for the heat power produced by Joule effect we have:

$$P_{ind} = \iiint_V p_{ind}\,\mathrm{d}^3r$$

$$P_{ind} \propto J_0^2 \propto I_0^2$$

with I_0 the amplitude of the current propagating inside the coils.

Hysteresis Power-Loss Heating (P_{hyst} / I^2 dependency)

In thermodynamics, the differential internal energy $\mathrm{d}U$ is written as follows:

$$\mathrm{d}U = \delta Q + \delta W$$

If we make the approximation of adiabatic conditions we have:

$$\mathrm{d}U = \delta W$$

the differential magnetic work is:

$$\delta W = \vec{H}\mathrm{d}\vec{B}$$

With $\vec{B}$ the magnetic field vector and $\vec{H}$ the magnetic field.
Then:

$$\mathrm{d}U = \vec{H}\mathrm{d}\vec{B}$$

$\vec{B}$ can be expressed as a function of $\vec{H}$ and the magnetization of the sample $\vec{M}$:

$$\vec{B} = \mu_0(\vec{H} + \vec{M})$$

With μ_0 the permeability of free space.

If we consider $\vec{B}$, $\vec{H}$ and $\vec{M}$ colinear, then we have:

$$B = \mu_0(H + M)$$

If we use the previous equation, we can write $\mathrm{d}U$ as:

$$\mathrm{d}U = \mu_0 H\mathrm{d}H + \mu_0 H\mathrm{d}M$$

Now we are interesting by the energy produced in one temporal cycle:

$$\Delta U = \oint \mathrm{d}U$$

$$\Delta U = \mu_0 \oint H\mathrm{d}H + \mu_0 \oint H\mathrm{d}M$$

$$\Delta U = \mu_0 \oint H\mathrm{d}M$$

After an integration by parts we can write:

$$\Delta U = -\mu_0 \oint M \mathrm{d}H$$

The magnetization can be expressed as a function of $\vec{H}$ and the complex magnetic susceptibility $\chi = \chi' - \mathrm{i}\chi''$:

$$H(t) = H_0 \cos(\omega t) = \Re(H_0 \mathrm{e}^{\mathrm{i}\omega t})$$

$$M(t) = \Re(\chi H_0 \mathrm{e}^{\mathrm{i}\omega t}) = H_0(\chi' \cos(\omega t) + \chi'' \sin(\omega t))$$

With ω the pulsation, which is link to the frequency by:

$$\omega = 2\pi f$$

Then the energy produced in one temporal cycle becomes:

$$\Delta U = \mu_0 \omega H_0^2 \chi'' \int_0^{2\pi/\omega} \sin^2(\omega t) \mathrm{d}t$$

$$\Delta U = \mu_0 \pi H_0^2 \chi''$$

The heat power produced by hysteresis power-loss heating effect is:

$$P_{hyst} = f \mu_0 \pi H_0^2 \chi''$$

From the precedent section, we know that H_0^2 is directly proportional to the current I_0 of the coils ($\vec{B} = \vec{\nabla} \wedge A$, and $\vec{B}$ colinear with $\vec{H}$). Then we have:

$$P_{hyst} \propto I_0^2$$

With I_0 the amplitude of the current propagating inside the coils.

III- Reactions performed using i-BM

a/ Reagents

The following commercial precursors were used as received without further purification: palmitic acid ($C_{16}H_{32}O_2$, Sigma-Aldrich, 99% purity, noted here PA), stearic acid ($C_{18}H_{36}O_2$, Sigma-Aldrich, 99% purity, noted here PA), behenic acid ($C_{22}H_{44}O_2$, Sigma-Aldrich, 99% purity, noted here BA), 1,1'-carbonyldiimidazole ($C_7H_6N_4O$, TCI, >97% purity, noted here CDI), L-leucine methyl ester hydrochloride ($C_7H_{15}NO_2 \cdot HCl$, Alfa Aesar, 99% purity), urea (CH_4N_2O), and silica (Aerosil 200, SiO_2, Degussa, 180 m^2/g, aggregated nanoparticles of ≈12 nm diameter). ^{18}O-labeled and ^{17}O-labeled waters (with 99.3% ^{18}O-enrichment and 39.3% ^{17}O-enrichment respectively) were purchased from CortecNet.

b/ Milling and ^{17}O-enrichment of silica

The milling and ^{17}O-labeling of silica was performed by adapting a previously published protocol.[2] In brief, first, two stainless steel milling balls (10 mm diameter) were introduced into a milling jar (10 mL inner volume). SiO_2 and ^{17}O-enriched water were then added, using a 1 : 1 molar ratio between these reagents. All samples were then milled in a Fritsch P23 mixer mill, using the experimental conditions listed in Table S3 (*i.e.* for 5 or 15 minutes of milling, with or without induction heating). After milling, the samples were recovered by gentle scratching of the jar and milling balls with a spatula, followed by drying under vacuum at ≈0.08 mbar at room temperature for 15 min to remove residual water. Dried samples were stored in glass vials (caps covered with parafilm), which were placed in a freezer in a container with drying beads. Before any characterization or further analysis, samples were taken out for 30 min to warm up to room temperature.

Entry	SiO_2 mass (mg)	$H_2{}^{17}O$ (µL)	Number of balls	Milling time (min)	Milling frequency (Hz)	Milling temperature
1	101.4	30	2	5	25	≈65°C
2	101.6	30	2	5	25	RT
3	101.9	30	2	15	25	≈65°C
4	101.8	30	2	15	25	RT

Table S3. Reagent quantities and milling conditions used for the ^{17}O-labeling of silica, with or without i-BM (RT = room temperature).

At 14.1 T, ^{17}O MAS NMR spectra were acquired on a Varian VNMRS spectrometer using Varian 3.2 mm HXY or PhoenixNMR probes, operating at a ^{17}O frequency of 81.31 MHz and ^{1}H frequency of 599.82 MHz. The spinning frequency was controlled at 16 kHz. The double frequency sweep (DFS) was used for ^{17}O signal enhancement.[3] The parameters were as follows: DFS pulse of 500 μs (RF≈10 kHz), swept between 200 and 80 kHz, and followed by an echo, with of 2.0 and 4.0 μs pulses, and an echo delay of 500 μs (8 rotor periods). Pulses were calibrated using the nutation curve of liquid water, for which the 90° pulse was 6.0 μs (RF 41.6 kHz). The recycle delay was set to 0.5 s, and the number of transients acquired was 8000. ^{17}O chemical shifts were referenced using tap water at 0.0 ppm (which corresponds to D_2O at −2.7 ppm).

N_2 volumetric analyses were conducted by physisorption of N_2 using a Tristar instrument (Micromeritics, Norcross, GA). Samples were degassed at 150 °C under vacuum overnight before measurements. Specific surface areas were derived from the isotherms using the Brunauer-Emmett-Teller (BET) method, and the distribution in pore diameters was plotted as a function of the pore volume, by analyzing the desorption data using the Barrett-Joyner-Halenda (BJH) method, in line with our previous work.[2] Errors on the surface areas for samples prepared under similar conditions were estimated to be ±20 $m^2 g^{-1}$.

c/ Hydrolysis of activated fatty acids

The hydrolysis of CDI-activated fatty acids was performed by adapting previously published protocols.[4,5] First, the activation step was performed at room temperature in a MM400 mixer mill operated at 25 Hz, using the quantities reported in Table S4. In brief, the fatty acid (1.0 eq) and CDI (1.1 eq) were introduced into a stainless-steel grinding jar (50 mL inner volume) containing eight stainless-steel balls (10 mm diameter). The jar was closed and subjected to grinding for several minutes (PA: 60 min; SA: 90 min; BA: 120 min) in the MM400 mixer mill operated at 25 Hz. The activated mixture was analysed by IR spectroscopy, as shown in main text (Figure 5, green spectra). The melting points of the activated mixtures were also determined, and found to be equal to ≈73, 78 and 90 °C for palmitic, stearic, and behenic acids, respectively.

	Activation (MM400, 25 Hz)			**Hydrolysis (P23, 30 Hz)**			
FA	**FA mass (mg)**	**CDI mass (mg)**	**Milling time (min)**	**Activated FA mixture mass (mg)**	**H_2O volume (µL)**	**Milling time (min)**	**Milling temperature**
Palmitic acid (PA)	556.8	386.9	60	105.6	≈14	60	RT
	556.4	386.3	60	101.7	≈14	15	≈70°C
	556.9	383.1	60	102.0	≈14	5	≈70°C
Stearic acid (SA)	462.8	289.2	90	101.8	≈14	60	RT
	463.6	288.2	90	105.3	≈14	15	≈85°C
	469.6	288.7	90	103.4	≈14	5	≈85°C
Behenic acid (BA)	465.4	244.1	120	100.8	≈12	60	RT
	464.5	243.9	120	103.9	≈12	15	≈90°C

Table S4. Reagent quantities and milling conditions used for the CDI-activation and subsequent hydrolysis of fatty acids, with or without i-BM (RT = room temperature).

For the hydrolysis step, a part of the activated mixture (≈100 mg) was then collected (for PA ≈100 mg of activated mixture contains ≈80%wt of activated acid form, *i.e.* ≈0.25 mmol), and introduced in a P23 stainless-steel grinding jar with two stainless-steel balls (10 mm diameter). Water (≈14 µL for PA, *i.e.* ≈3.0 eq) was then added into the jar using a microseringe. The jar was closed, placed in the middle of the induction coil (as shown in Figure S1), and the mixture was subjected to further grinding for 5 to 60 minutes at 30 Hz, either at room temperature or using i-BM (see Table S4 for specific labeling conditions). The medium, which has a liquid state, was then analysed by FTIR. To help recover the product, non-labeled water (1 mL) was added into the jar, and the content was subjected to grinding for 2 minutes at 25 Hz. Then, the medium ("milky" solution with a foam on top) was transferred to a beaker (together with a sufficient amount of non-labeled water, *i.e.* 10-15 mL, used here to rinse the jar), poured into a separatory funnel, diluted and acidified with an aqueous solution of HCl (1M, 15 mL), and finally extracted with ethyl acetate (1x20 mL, 2x10 mL). Combined organic phases were dried over Na_2SO_4, filtered, and finally dried under vacuum to yield the product as white microcrystalline solid, which was analysed by IR, ^1H solution NMR and mass spectrometry.

Infrared (IR) spectra were recorded on a Perkin Elmer Spectrum 2 FT-IR spectrometer, using the ATR measurement mode (4000 – 400 cm^{-1} range, 4 repetitions). Mass spectrometry analyses were performed on a Waters Synapt G2-S apparatus (electrospray ionization in negative mode in a range of 50-1500 Da), using methanol as a solvent, and similar measurement conditions as in our previous work.[4] ^1H solution NMR spectra were recorded on an Avance III Bruker 600 MHz NMR spectrometer equipped with a TCI Prodigy cryoprobe, using DMSO-d_6 as a solvent. Chemical shifts were referenced to the residual solvent peak at 2.50 ppm. Melting points of the activated mixtures were measured on BÜCHI Melting Point B-540 instrument with two successive heating rates: the first of 5 °C/min to approach the theoretical melting point of the corresponding FA, and the second of 1 °C/min to precisely determine the actual melting point of the activated mixture.

Characterizations of ^{17}O or ^{18}O-enriched palmitic, stearic and behenic acids, in comparison to the starting material, are shown in Figures S9, S10 and S11, respectively. Moreover, comparisons of the hydrolysis of activated palmitic and stearic acid after 5 and 15 min BM are shown in Figures S12 and S13.

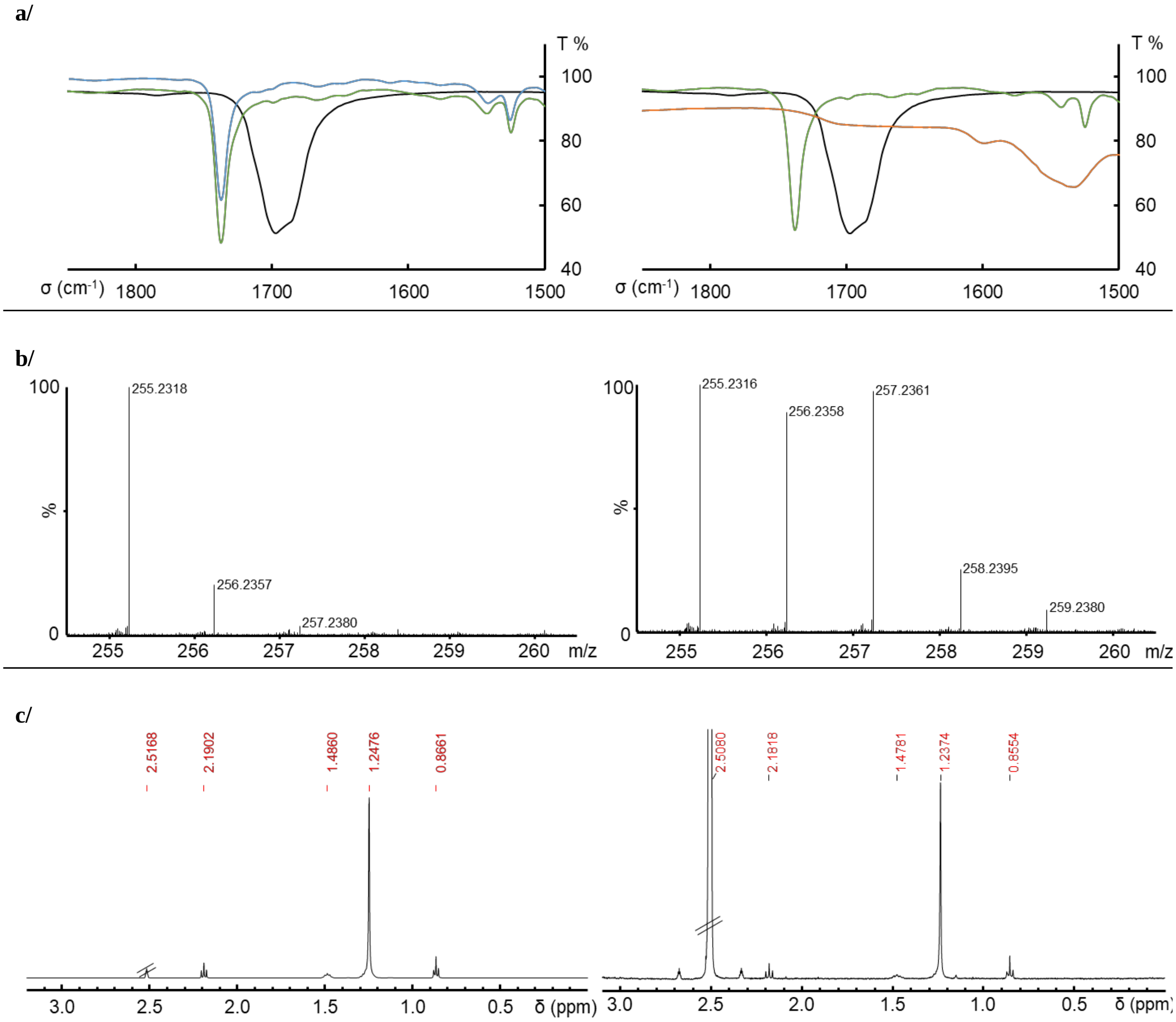

Figure S9. Characterizations of non-labeled (left) and ^{17}O-labeled (right) palmitic acid (PA), prepared using i-BM (5 min milling during the hydrolysis), by (a) IR spectroscopy (Black, PA ; Green, activated PA ; Blue, 60 min RT-BM “hydrolysis” ; Orange, 5 min i-BM hydrolysis), (b) mass spectrometry (ESI, negative mode) and (c) ^{1}H solution NMR.

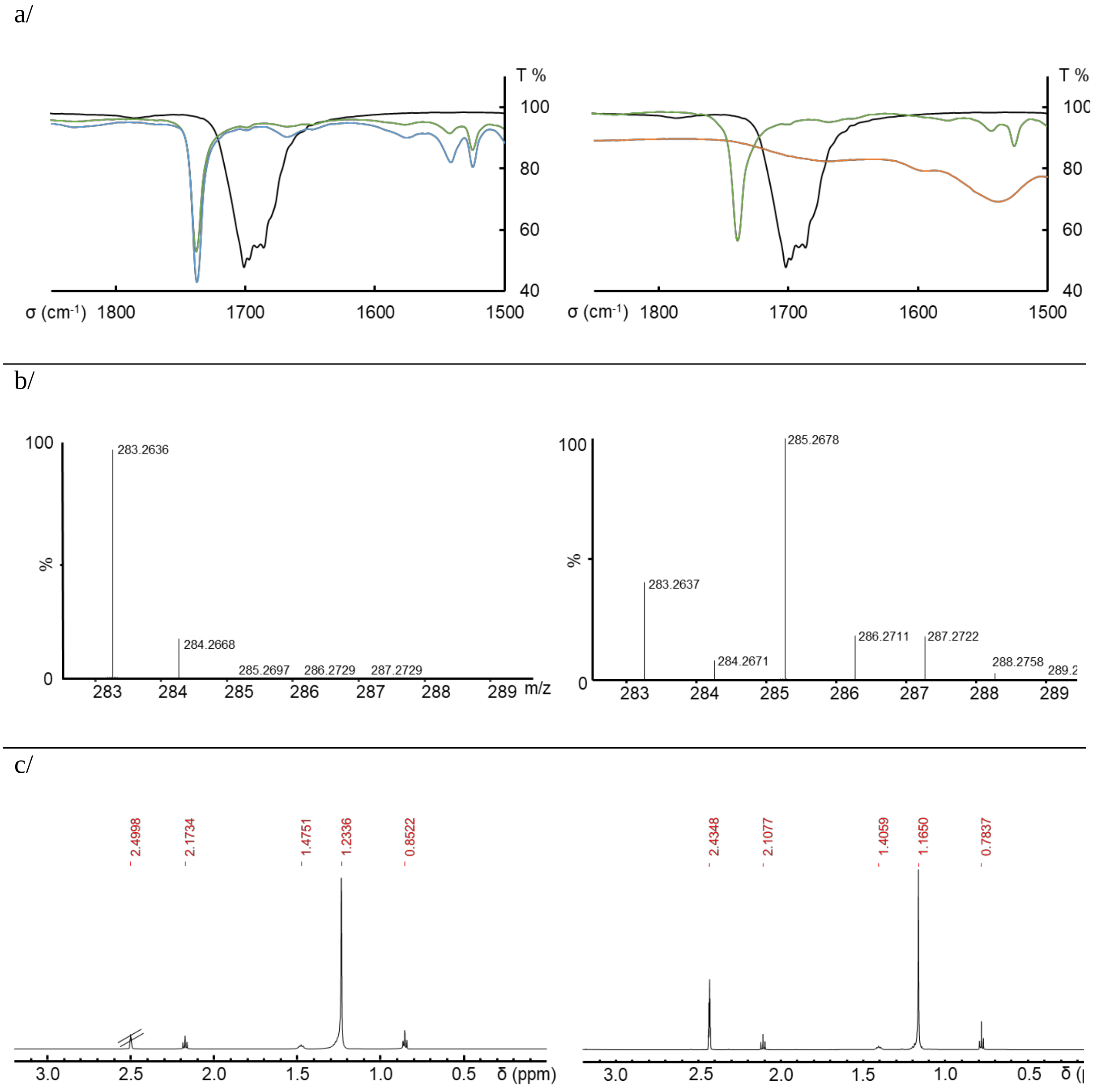

Figure S10. Characterizations of non-labeled (left) and ^{18}O-labeled (right) stearic acid (SA), prepared using i-BM (15 min milling during the hydrolysis), by (a) IR spectroscopy (Black, SA ; Green, activated SA ; Blue, 60 min RT-BM "hydrolysis" ; Orange, 15 min i-BM hydrolysis), (b) mass spectrometry (ESI, negative mode) and (c) ^{1}H solution NMR.

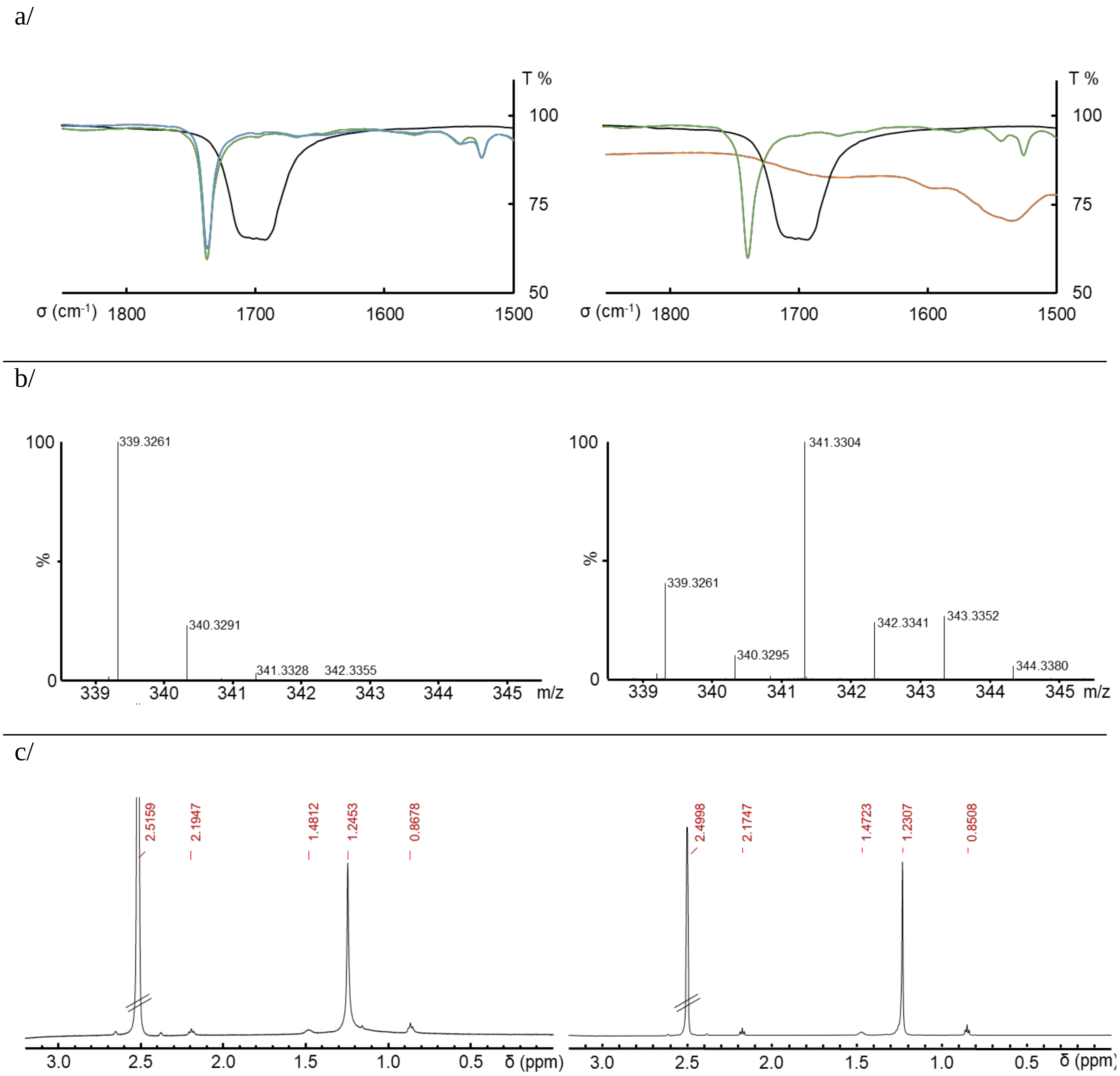

Figure S11. Characterizations of non-labeled (left) and ^{18}O-labeled (right) behenic acid (BA), prepared using i-BM (15 min milling during the hydrolysis), by (a) IR spectroscopy (Black, BA ; Green, activated BA ; Blue, 60 min RT-BM "hydrolysis" ; Orange, 15 min i-BM hydrolysis), (b) mass spectrometry (ESI, negative mode) and (c) ^{1}H solution NMR.

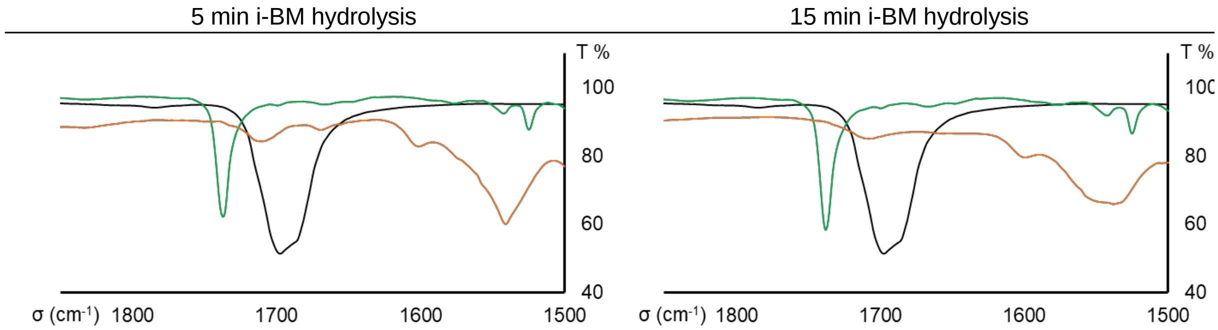

Figure S12. Comparisons of the IR spectra after hydrolysis of PA using ultrapure water, after 5 (left) and 15 (right) minutes of i-BM, as shown by IR spectroscopy (Black, PA ; Green, activated PA ; Orange, i-BM hydrolysis)

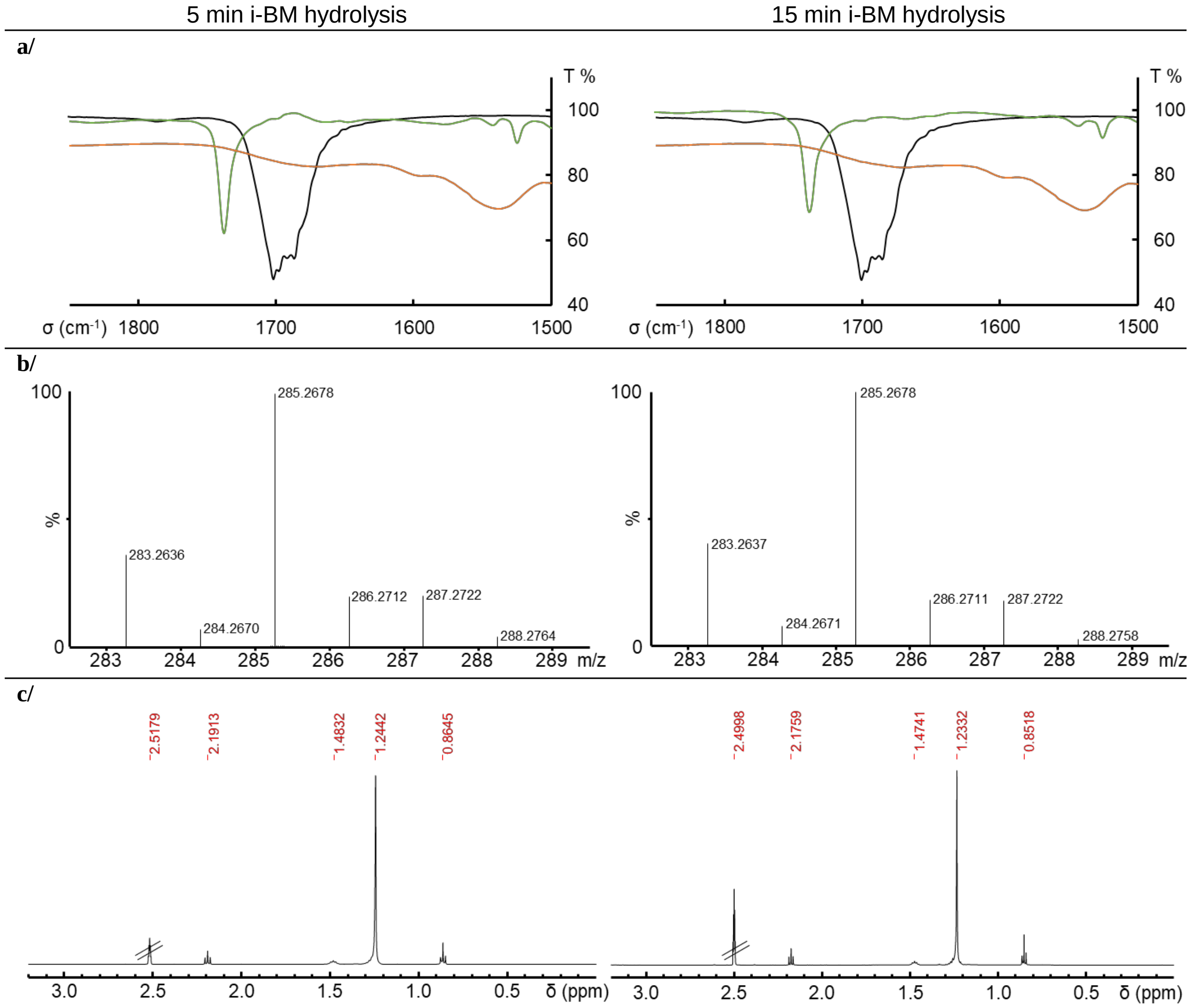

Figure S13. Comparisons of the products isolated by hydrolysis of activated SA using ^{18}O-labeled water, after 5 (left) and 15 (right) minutes of i-BM, as shown by (a) IR spectroscopy (Black, SA ; Green, activated SA ; Orange, i-BM hydrolysis), (b) mass spectrometry (ESI, negative mode), and (c) ^{1}H solution NMR.

d/ Formation of “snowballs”: synthesis of the leucine methyl ester-urea cocrystal

First, L-leucine methyl ester hydrochloride (375.8 mg, 2.0 mmol, 1 eq.) was introduced into a Perspex (PMMA) P23 reactor, followed by urea (124.2 mg, 2.0 mmol, 1 eq.), for a total mass of 500 mg. Then, two 10 mm diameter stainless-steel beads were added before closing the reactor (parafilm was added to cover the junction of top/bottom parts). The system was then subjected to grinding for ~2-4 min in the P23 mixer mill operating at 50 Hz. In absence of heating, the appearance of the snowball effect on the surface of the stainless-steel beads was observed, which disrupted the milling process. When triggering the induction heating (i-BM) for a target temperature 85°C, the progressive “melting” of the snowball was noticed, the sticky reaction mixture becoming spread on the reactor’s walls (see video made available in supporting materials).

Melting points were measured using a Büchi Melting point B-540 apparatus, and found to be equal to 133-135°C, 151-153°C, and 87-92°C for urea, L-leucine methyl ester hydrochloride and the co-crystal, respectively. Powder XRD analyses were performed on an X’Pert MPD diffractometer using Cu Kα1 radiation ($\lambda = 1.5406$ Å) with the operation voltage and current maintained at 40 kV and 25 mA, respectively. Diffractograms were recorded between $2\theta = 5°$ and $50°$ in Bragg-Brentano configuration, with a step size of 0.050°, and a time per step of 60 s.

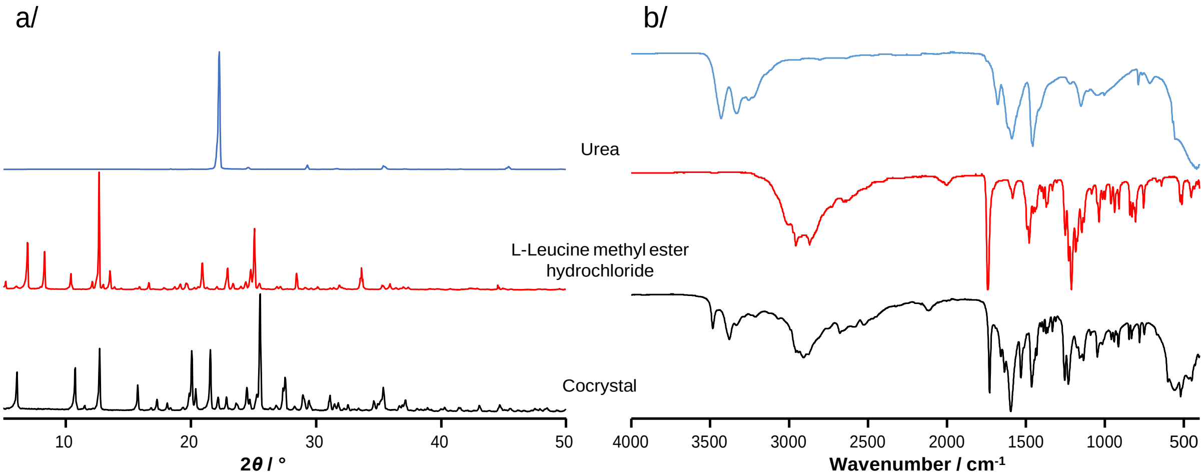

Figure S14. a/ Powder X-ray diffractograms, and b/ IR spectra, of urea (blue), L-leucine methyl ester hydrochloride (red) and the cocrystal (black).

IV- More complete literature survey on combined heating & milling studies

Table S5. Different experimental approaches proposed in the literature to combine heating and milling (as of September 2022)

Heating system	**Advantages**	**Drawbacks**	**References**
Most frequently described systems			
Heated fluid circulating around the jar (*e.g.* with a double walled beaker) [a]	• Good temp. control	• External heating only • Limited to thermally conducting jars • Not adapted for *operando* measurements	[6–11]
Heating tape/band	• Good temp. control • Possibility to do heating cycles with different high-temp. plateaus	• External heating only • Limited to thermally conducting jars • Not adapted for *operando* measurements in most cases	[12–21,b]
Heat gun	• Moderate to good temp. control • Relatively simple set-up	• External heating only (through air) • Potentially inhomogeneous heating • Limited to thermally conducting jars • Not adapted for Raman/XRD *operando* measurements	[20,22–28]
Less frequently described systems			
Heated fluid circulating around the jar (*e.g.* with Retsch MM500 design)	• Good temp. control • Heating and cooling (-100 +100 °C) • Commercially available • Pressure up to 5 bars	• Limited to +100 °C • External heating only • Limited to thermally conducting jars • Not adapted for *operando* measurements	[29]
Furnace/Oven [a]	• Good temp. control	• External heating only • Limited to thermally conducting jars • Not adapted for *operando* analyses	[19,30,31,b]
Jar placed in rotary evaporator bath	• Good temp. control	• Low-energy milling • External heating only • Limited to round-bottom flasks • Not adapted for *operando* analyses	[9]
Microwave source	• Possibility for internal heating (not described)	• Low-energy milling • Need for a microwave-receptive material	[9]
Induction-assisted continuous grinder (WAB IMPA°CT)	• Possibility for internal heating • Heating up to 160 °C	• Patented system • Not designed to be adaptable to most frequent lab mills	[32,33]

[a] Systems with limited description available in the literature.

[b] It is not clear to us whether reference [19] is using a heating tape or an IR-heating lamp.

REFERENCES

1 https://ultraflexpower.com/.

2 C.-H. Chen, F. Mentink-Vigier, J. Trébosc, I. Goldberga, P. Gaveau, E. Thomassot, D. Iuga, M. E. Smith, K. Chen, Z. Gan, N. Fabregue, T. Métro, B. Alonso and D. Laurencin, Labeling and Probing the Silica Surface Using Mechanochemistry and ^{17}O NMR Spectroscopy, *Chem. – A Eur. J.*, 2021, **27**, 12574–12588.

3 F. A. Perras, J. Viger-Gravel, K. M. N. Burgess and D. L. Bryce, Signal enhancement in solid-state NMR of quadrupolar nuclei, *Solid State Nucl. Magn. Reson.*, 2013, **51–52**, 1–15.

4 J. Špačková, C. Fabra, G. Cazals, M. Hubert-Roux, I. Schmitz-Afonso, I. Goldberga, D. Berthomieu, A. Lebrun, T.-X. Métro and D. Laurencin, Cost-efficient and user-friendly ^{17}O/ ^{18}O labeling procedures of fatty acids using mechanochemistry, *Chem. Commun.*, 2021, **57**, 6812–6815.

5 J. Špačková, C. Fabra, S. Mittelette, E. Gaillard, C.-H. Chen, G. Cazals, A. Lebrun, S. Sene, D. Berthomieu, K. Chen, Z. Gan, C. Gervais, T.-X. Métro and D. Laurencin, Unveiling the Structure and Reactivity of Fatty-Acid Based (Nano)materials Thanks to Efficient and Scalable ^{17}O and ^{18}O-Isotopic Labeling Schemes, *J. Am. Chem. Soc.*, 2020, **142**, 21068–21081.

6 G. Kaupp, How are Waste Entirely Avoided in Solid-State Productions?, *J. Chem. Eng. Process Technol.*, 2017, **08**, 1000335.

7 G. Kaupp, Solid-state molecular syntheses: complete reactions without auxiliaries based on the new solid-state mechanism, *CrystEngComm*, 2003, **5**, 117.

8 S. Mashkouri and M. Reza Naimi-Jamal, Mechanochemical Solvent-Free and Catalyst-Free One-Pot Synthesis of Pyrano[2,3-d]Pyrimidine-2,4(1H,3H)-Diones with Quantitative Yields, *Molecules*, 2009, **14**, 474–479.

9 R. Schmidt, C. F. Burmeister, M. Baláž, A. Kwade and A. Stolle, Effect of Reaction Parameters on the Synthesis of 5-Arylidene Barbituric Acid Derivatives in Ball Mills, *Org. Process Res. Dev.*, 2015, **19**, 427–436.

10 G. Kaupp, M. R. Naimi-Jamal and V. Stepanenko, Waste-Free and Facile Solid-State Protection of Diamines, Anthranilic Acid, Diols, and Polyols with Phenylboronic Acid, *Chem. - A Eur. J.*, 2003, **9**, 4156–4161.

11 J. Andersen and J. Mack, Insights into Mechanochemical Reactions at Targetable and Stable, Sub-ambient Temperatures, *Angew. Chemie Int. Ed.*, 2018, **57**, 13062–13065.

12 J. M. Andersen and J. Mack, Decoupling the Arrhenius equation via mechanochemistry, *Chem. Sci.*, 2017, **8**, 5447–5453.

13 J. M. Andersen and H. F. Starbuck, Rate and Yield Enhancements in Nucleophilic Aromatic Substitution Reactions via Mechanochemistry, *J. Org. Chem.*, 2021, **86**, 13983–13989.

14 S. Immohr, M. Felderhoff, C. Weidenthaler and F. Schüth, An Orders-of-Magnitude Increase in the Rate of the Solid-Catalyzed CO Oxidation by In Situ Ball Milling, *Angew. Chemie Int. Ed.*, 2013, **52**, 12688–12691.

15 G. Báti, D. Csókás, T. Yong, S. M. Tam, R. R. S. Shi, R. D. Webster, I. Pápai, F. García and M. C. Stuparu, Mechanochemical Synthesis of Corannulene-Based Curved Nanographenes, *Angew. Chemie Int. Ed.*, 2020, **59**, 21620–21626.

16 J. Andersen, H. Starbuck, T. Current, S. Martin and J. Mack, Milligram-scale, temperature-controlled ball milling to provide an informed basis for scale-up to reactive extrusion, *Green Chem.*, 2021, **23**, 8501–8509.

17 N. Cindro, M. Tireli, B. Karadeniz, T. Mrla and K. Užarević, Investigations of Thermally Controlled Mechanochemical Milling Reactions, *ACS Sustain. Chem. Eng.*, 2019, **7**, 16301–16309.

18 I. Brekalo, V. Martinez, B. Karadeniz, P. Orešković, D. Drapanauskaite, H. Vriesema, R. Stenekes, M. Etter, I. Dejanović, J. Baltrusaitis and K. Užarević, Scale-Up of Agrochemical Urea-Gypsum Cocrystal Synthesis Using Thermally Controlled Mechanochemistry, *ACS Sustain. Chem. Eng.*, 2022, **10**, 6743–6754.

19 M. Bilke, P. Losch, O. Vozniuk, A. Bodach and F. Schüth, Methane to Chloromethane by Mechanochemical Activation: A Selective Radical Pathway, *J. Am. Chem. Soc.*, 2019, **141**, 11212–11218.

20 R. R. A. Bolt, S. E. Raby-Buck, K. Ingram, J. A. Leitch and D. L. Browne, Temperature-Controlled Mechanochemistry for the Nickel-Catalyzed Suzuki–Miyaura-Type Coupling of Aryl Sulfamates via Ball Milling and Twin-Screw Extrusion., *Angew. Chemie Int. Ed.*, 2022, e202210508.

21 K. Linberg, B. Röder, D. Al-Sabbagh, F. Emmerling and A. A. L. Michalchuk, Controlling polymorphism in molecular cocrystals by variable temperature ball milling, *Faraday Discuss.*, 2023, **241**, 178–193.

22 R. Takahashi, A. Hu, P. Gao, Y. Gao, Y. Pang, T. Seo, J. Jiang, S. Maeda, H. Takaya, K. Kubota and H. Ito, Mechanochemical synthesis of magnesium-based carbon nucleophiles in air and their use in organic synthesis, *Nat. Commun.*, 2021, **12**, 6691.

23 P. Gao, J. Jiang, S. Maeda, K. Kubota and H. Ito, Mechanochemically Generated Calcium-Based Heavy Grignard Reagents and Their Application to Carbon–Carbon Bond-Forming Reactions, *Angew. Chemie Int. Ed.*, 2022, **61**, e202207118.

24 T. Seo, N. Toyoshima, K. Kubota and H. Ito, Tackling Solubility Issues in Organic Synthesis: Solid-State Cross-Coupling of Insoluble Aryl Halides, *J. Am. Chem. Soc.*, 2021, **143**, 6165–6175.

25 R. Takahashi, T. Seo, K. Kubota and H. Ito, Palladium-Catalyzed Solid-State Polyfluoroarylation of Aryl Halides Using Mechanochemistry, *ACS Catal.*, 2021, **11**, 14803–14810.

26 Y. Gao, C. Feng, T. Seo, K. Kubota and H. Ito, Efficient access to materials-oriented aromatic alkynes via the mechanochemical Sonogashira coupling of solid aryl halides with large polycyclic conjugated systems, *Chem. Sci.*, 2022, **13**, 430–438.

27 K. Kubota, T. Endo, M. Uesugi, Y. Hayashi and H. Ito, Solid-State C−N Cross-Coupling Reactions with Carbazoles as Nitrogen Nucleophiles Using Mechanochemistry, *ChemSusChem*, 2022, 15, e202102132.

28 J. Zhang, P. Zhang, Y. Ma and M. Szostak, Mechanochemical Synthesis of Ketones via Chemoselective Suzuki–Miyaura Cross-Coupling of Acyl Chlorides, *Org. Lett.*, 2022, **24**, 2338–2343.

29 https://www.retsch.fr/fr/produits/broyer/broyeurs-a-billes/mm-500-control/.

30 R. Eckert, M. Felderhoff and F. Schüth, Preferential Carbon Monoxide Oxidation over Copper-Based Catalysts under In Situ Ball Milling, *Angew. Chemie Int. Ed.*, 2017, **56**, 2445–2448.

31 K. L. Chagoya, D. J. Nash, T. Jiang, D. Le, S. Alayoglu, K. B. Idrees, X. Zhang, O. K. Farha, J. K. Harper, T. S. Rahman and R. G. Blair, Mechanically Enhanced Catalytic Reduction of Carbon Dioxide over Defect Hexagonal Boron Nitride, *ACS Sustain. Chem. Eng.*, 2021, **9**, 2447–2455.

32 J. Thiel, F. Lacoste, V. Lair, S. Halloumi, I. Malpartida, B. Moevus, Three-dimensional grinder, method for implementing same and uses thereof. **2019**, WO2019228983A1.

33 https://impact-reactor.wab-group.com/.